Letter

Evidence for near-unity radiative quantum efficiency of bright excitons in carbon nanotubes from the Purcell effect

H. Machiya,[1,2] D. Yamashita,[3] A. Ishii,[1,3] and Y. K. Kato[1,3,*]

[1]*Nanoscale Quantum Photonics Laboratory, RIKEN Cluster for Pioneering Research, Saitama 351-0198, Japan*
[2]*Department of Electrical Engineering, The University of Tokyo, Tokyo 113-8656, Japan*
[3]*Quantum Optoelectronics Research Team, RIKEN Center for Advanced Photonics, Saitama 351-0198, Japan*

(Received 19 March 2021; revised 27 February 2022; accepted 23 March 2022; published 15 April 2022)

The efficiencies of photonic devices are primarily governed by radiative quantum efficiency, which is a property given by the light-emitting material. Quantitative characterization for carbon nanotubes, however, has been difficult despite being a prominent material for nanoscale photonics. Here we estimate the radiative quantum efficiency of bright excitons in carbon nanotubes by modifying the exciton dynamics through cavity quantum electrodynamical effects. Silicon photonic crystal nanobeam cavities are used to induce the Purcell effect on individual carbon nanotubes. Spectral and temporal behavior of the cavity enhancement is characterized by photoluminescence microscopy and the fraction of the radiative decay process is evaluated. We find that the radiative quantum efficiency can reach near unity for bright excitons in long air-suspended carbon nanotubes at room temperature.

DOI: 10.1103/PhysRevResearch.4.L022011

Radiative quantum efficiency is a fundamental physical quantity that ultimately limits the efficiency of optoelectronic devices. Type III-V direct gap semiconductors with radiative quantum efficiencies close to 100% have played a central role in the development of efficient light emitting diodes (LEDs) that are now used ubiquitously [1]. Modern high-power diode lasers see extensive use in industries including telecommunications [2], materials processing, and medical treatments [3], but the performance needed for broad applications would have not been possible without the high quantum efficiencies of the gain materials. Organic semiconductors have likewise seen commercial success in LED displays [4], but only after substantial improvement of their radiative quantum efficiencies [5,6].

Carbon nanotubes (CNTs), also as a direct gap semiconductor, have demonstrated their potential as a key material for nanoscale photonic devices. Electrically gated *pn*-junction devices can be constructed from nanotubes with diameters significantly smaller than the wavelength, where extremely efficient photocurrent generation [7,8] and excitonic electroluminescence [9,10] have been demonstrated. Unique exciton physics can be exploited to generate telecom-band single photons at room temperature [11–13], and the compatibility of nanotube emitters with silicon photonics [14–19] offers opportunities in integrated quantum optics [20]. The device performance is again limited by the radiative quantum efficiency, but the uncertainty of absorption cross section and sensitivity to nanotube quality have made quantitative characterization difficult.

Here we experimentally estimate the radiative quantum efficiencies of excitons in air-suspended CNTs. Quantum electrodynamical effects in nanoscale photonic cavities are used to selectively modify the radiative decay rate of excitons, allowing us to gain insight to the fractions of radiative and nonradiative processes before the modification. Individual CNTs are coupled to air-mode photonic crystal nanobeam cavities, and photoluminescence (PL) measurements are performed to quantitatively evaluate the spectral and temporal enhancements induced by the Purcell effect. We find that the radiative quantum efficiency can reach near unity for bright excitons in long air-suspended carbon nanotubes at room temperature. Statistically, 40% of nanotubes are found to exhibit radiative quantum efficiencies larger than 70%.

Microcavities alter the decay dynamics of excitons through a quantum electrodynamical phenomenon known as the Purcell effect [21]. In free space, the total exciton decay rate can be written as $\gamma_r + \gamma_{nr}$ where γ_r and γ_{nr} are the radiative and nonradiative decay rates, respectively. When excitons are coupled to a microcavity, the increased photon density of states gives rise to an additional radiative decay rate $F\gamma_r$, where F is the Purcell factor [14–17,22,23]. Combined with the unchanged free-space emission, the resulting total radiative decay rate within the microcavity is then given by $(1 + F)\gamma_r$. The accelerated radiative recombination appears in the spectral domain as an increased intensity in a spectrally narrow region around the cavity resonance. If the radiative quantum efficiency $\eta = \gamma_r/(\gamma_r + \gamma_{nr})$ is low, the Purcell effect also increases the radiative fraction of the recombination. The acceleration is more directly observed in the time domain as a shortening in the lifetime. The overall change in the decay

*Corresponding author: yuichiro.kato@riken.jp

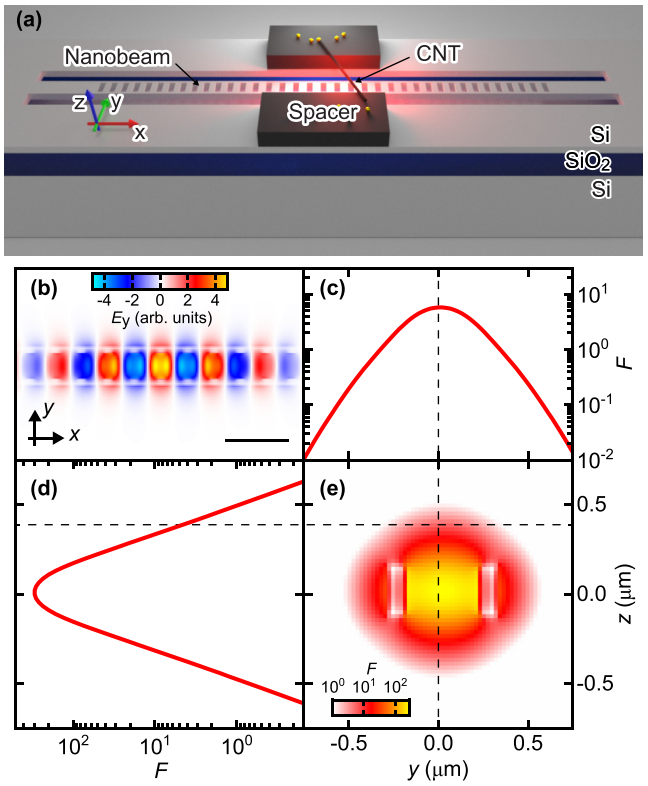

FIG. 1. (a) Schematic of the device. (b) Simulated spatial distribution of the y component of the electric field E_y for the fundamental transverse-electric mode at $z = 0.00\,\mu$m. The lattice constant $a =$ 350 nm is used and the cavity center period is $1.18a$. The beam width is 600 nm and the holes are 140 nm by 400 nm. The Si layer thickness of 260 nm is chosen to match the actual devices. The scale bar is 1 μm. (c)–(e) Spatial profiles of the calculated Purcell factor at $x = 0.00\,\mu$m. Cross sections through the dashed lines at (c) $z = 0.38\,\mu$m and (d) $y = 0.00\,\mu$m. Position-dependent Purcell factor is calculated from $F(\vec{r}) = \frac{3}{4\pi^2}\frac{Q}{V}\lambda^3|E_y(\vec{r})|^2/\max|E_y(\vec{r})|^2$, where Q is the emitter quality factor, V is the mode volume, and $E_y(\vec{r})$ is the y component of the electric field amplitude at position $\vec{r}$. For (b)–(e), The coordinate origin is taken to be the center of the cavity.

rate can be characterized by the acceleration factor defined as the enhancement of the total decay rate by the Purcell effect

$$A = \frac{(1+F)\gamma_r + \gamma_{nr}}{\gamma_r + \gamma_{nr}} = 1 + F\eta. \tag{1}$$

If F and A are known, Eq. (1) allows us to estimate η without making further assumptions. By performing spectral- and time-domain measurements on excitons coupled to a microcavity, we independently evaluate the Purcell factor and the acceleration factor.

As our primary interest is in the intrinsic properties of excitons, we use as-grown air-suspended CNTs for the determination of the quantum efficiency. These tubes are known to exhibit high PL yields, indicative of their pristine nature [24]. To modify the radiative decay rates by the Purcell effect, the air-suspended tubes are coupled to silicon photonic crystal nanobeam cavities [14,17] as shown in Fig. 1(a). We utilize air-mode cavities characterized by ultrasmall mode volumes and large electric fields in the air holes, which allows for high-efficiency coupling [14].

The cavities are designed by finite-difference time-domain (FDTD) simulations [25]. We place 39 rectangular holes in an air-bridge nanobeam structure (see Supplemental Material Fig. S1 [26]), and the periodicity is increased at the cavity center in a parabolic manner over 16 periods [14]. The mode profile is presented in Fig. 1(b), where the large fields in the air holes can be seen. The cavity has a resonant wavelength $\lambda =$ 1460 nm and its quality factor and mode volume are calculated to be 4×10^5 and $0.025 \times \lambda^3$, respectively.

Because CNTs suffer from strong quenching effect upon contact with the substrate [27,28], we place spacer layers to suspend the tubes a few hundred nanometers above the cavity. The thickness of the spacers is critical in our device design since the evanescent fields of the cavity mode decreases exponentially above the cavity [Figs. 1(c) to 1(e)]. Due to the ultrasmall mode volume of the cavity, a Purcell factor of 5.8 is still available even a few hundred nm above the cavity surface [Fig. 1(d), dashed line].

Based on the simulation results, we choose a spacer layer thickness of 250 nm to place CNTs at $z = 380$ nm for our devices and fabricate the cavities from a silicon-on-insulator wafer. The nanobeams are designed to be 800-nm wide and the hole width is fixed at 500 nm, where we chose the parameters to correct for fabrication errors. The lattice constant a is varied from 320 nm to 511 nm to cover a wide wavelength range from 1100 to 1600 nm for coupling to a variety of nanotube chiralities and the hole length is scaled to be $0.4a$. We begin by defining cavities and alignment marks by electron beam lithography, and the 260-nm-thick top Si layer is etched by inductively coupled plasma etcher. Another electron beam writing patterns the spacer regions, where Si is sputtered and subsequently lifted off. The 1-μm-thick buried oxide layer is then etched by hydrofluoric acid to form the air-bridge structure. We perform a final electron beam writing to define catalyst windows, and the completed chip is diced into 4-mm square chips. We finally synthesize the nanotubes by alcohol chemical vapor deposition [28]. A scanning electron micrograph of a device is shown in Fig. 2(a).

The devices are characterized with a home-built confocal microscope system [17,28]. Samples are mounted on a motorized three-dimensional feedback stage, allowing us to perform automated measurements over a large number of devices. A wavelength-tunable Ti:sapphire laser is used as an excitation source, and the beam is focused by an objective lens with a numerical aperture of 0.85 and a focal length of 1.8 mm. Emission is collected with the same objective lens and coupled to a grating spectrometer with a liquid-nitrogen-cooled InGaAs photodiode array through a confocal pinhole corresponding to an aperture with 2.7-μm diameter at the sample image plane. Laser reflection is simultaneously collected and is monitored by a silicon photodiode to construct reflectivity images. Continuous-wave excitation is used unless otherwise noted and all measurements are performed at room temperature in a dry nitrogen environment.

As the chirality and the location of the nanotubes are randomly distributed, some effort is required to find tubes that have good spatial and spectral overlap with the cavity modes. To overcome the low yield of devices with optical coupling,

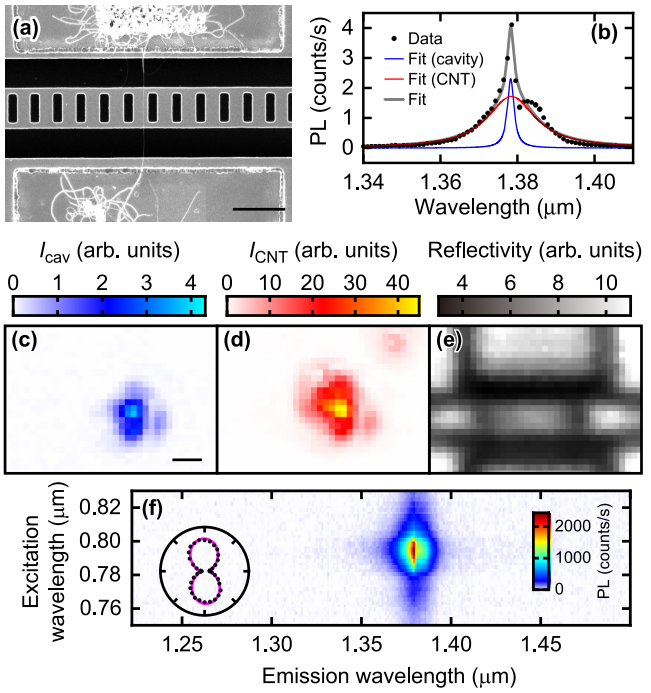

FIG. 2. (a) Scanning electron micrograph of a fabricated device. A CNT is suspended across the width of the trench near the center of the image. The scale bar is 1 μm. (b) Typical PL spectrum of a device showing optical coupling to the cavity. The dots are data and the gray line is the bi-Lorentzian fit. The blue and red curves correspond to the cavity and the CNT peak components, respectively. We interpret the asymmetry of the peak shape as a dip caused by the interference of the optics or the interference with the reflection from the bottom of the nanobeam substrate. (c,d) PL images for the (c) cavity and (d) CNT emission, obtained by mapping out the peak areas for each peak. (e) Reflectivity image taken simultaneously with (c) and (d). The scale bar in (c) is 1 μm and is shared between panels (c)–(e). For (b)–(e), the excitation laser wavelength is 793 nm and the laser polarization is parallel to the nanotube axis. (f) PL excitation map for the same device, taken with the laser polarization perpendicular to the nanobeam axis. Chirality is assigned to (9,8) using tabulated data [28]. Inset: Excitation polarization dependence of PL at 1378 nm with a spectral integration window of 5 nm. The dots are data and the line is a fit by cosine squared. (b)–(f) are taken with an excitation power of 20 μW.

which is typically less than 0.1%, more than 300 000 devices in total are prepared. Automated scanning is performed to efficiently collect PL spectra from a large number of devices, constructing colormaps of PL intensity as a function of position and wavelength (see Supplemental Material Fig. S2 [26]). The signature of optical coupling is the spectrally narrow peak corresponding to the cavity mode. We perform two-dimensional peak detection to extract such data and then nonlinear curve fitting is used to determine the linewidths for each peak. We select devices for detailed characterization when the linewidth is below 5 nm, sufficiently narrower than the typical linewidths of nanotubes.

Figure 2(b) shows a PL spectrum of a representative device, where a sharp peak corresponding to the cavity mode can be seen on top of a broader peak from CNT emission into free space. The cavity peak is centered at 1378.1 nm (0.90 eV) and has a linewidth of 0.5 nm (0.3 meV), whereas the CNT peak has a center wavelength of 1378.4 nm (0.90 eV) with a linewidth of 14.1 nm (9.2 meV). The cavity linewidth is limited by the spectrometer resolution and a separate measurement was performed to evaluate the actual value and the quality factor (see Supplemental Material Fig. S3 [26]). The cavity peak area I_{cav} and the CNT peak area I_{CNT} can be extracted using bi-Lorentzian fitting and a two-dimensional PL scan is performed to map out the spatial extent of the two components [Figs. 2(c) and 2(d)]. A reflectivity image is simultaneously taken and is shown in Fig. 2(e), which shows the location of the cavity. The profile of the cavity emission is predominantly localized at the center of the device, as expected from the electric field distribution of the cavity mode [Fig. 2(c)]. In comparison, the nanotube peak component extends beyond the width of the nanobeam, showing emission from the full length of the suspended nanotube [Fig. 2(d)]. We further characterize the device to ensure that the tube is individual and clean. A PL excitation map is used to identify the chirality, whereas the angle of the nanotube is obtained from polarization dependence of PL [Fig. 2(f)]. Devices showing multiple peaks or temporal instabilities are eliminated from further measurements, as they indicate bundling or contamination [29,30]. After such rigorous characterization, the number of devices that can be used for determining the quantum efficiency is less than 20 out of the 300 000 devices.

The Purcell factor is extracted from the PL spectrum taken at the center of the device [Fig. 2(b)], using the PL intensities of the two peak components. Letting C_{cav} and C_{CNT} be the collection efficiencies of the cavity mode and the nanotube emission, respectively,

$$F = \frac{I_{cav}/C_{cav}}{I_{CNT}/C_{CNT}}. \quad (2)$$

The collection efficiencies therefore have a critical effect on the value of F and are obtained using the radiation patterns from FDTD simulations (see Supplemental Material Sec. S4 [26]). For C_{cav}, we place a resonant source at the cavity center to compute the cavity radiation pattern [Fig. 3(a)]. Since the cavity mode primarily consists of zone boundary waveguide modes [Fig. 3(b)], coupling to leaky modes above the light line is small [31]. Most of the light that leaks out is directed at a low angle along the nanobeam, likely because most of the coupling occurs near the light line. As a result, only a small fraction of cavity photons fits within the numerical aperture of the objective lens, giving $C_{cav} = 0.15$. We calculate the nanotube radiation pattern in a similar manner, but the off-resonant excitation source is placed at the node of the mode profile and is spectrally detuned by 26 nm. In contrast to the cavity radiation pattern, the nanotube radiation is reduced by the photonic band gap at low angles, causing the emission to be redirected upward and increasing the collection efficiency to 40% [Fig. 3(c)]. In addition to the collection efficiency of the objective lens, we also include a correction factor in C_{CNT} to take into account the emission from the length of the tube beyond the width of the nanobeam. The additional factor is given by the entire length of the tube normalized with respect to the spatial width of the cavity mode. The entire tube length

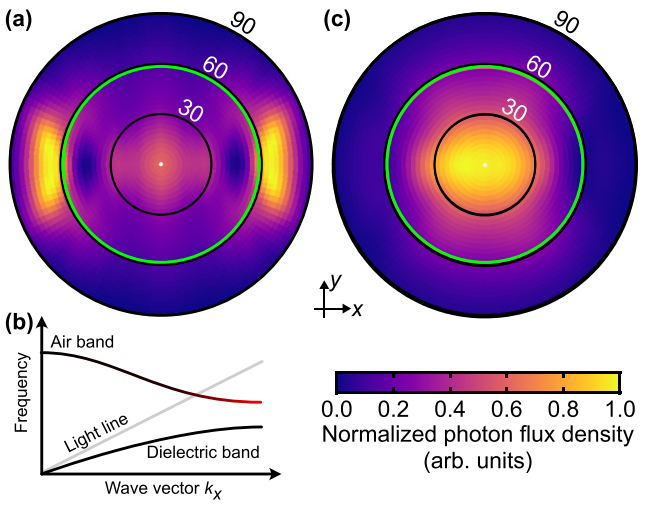

FIG. 3. (a) Calculated far-field radiation pattern of the fundamental cavity mode. (b) Schematic showing the photonic band diagram of one-dimensional photonic crystal. The red colored region of the air band represents the zone-boundary waveguide mode. (c) Calculated far-field radiation pattern of the uncoupled nanotube emission. For (a) and (c), photon flux density is plotted as a function of polar and azimuthal angles in spherical coordinates. The radial axis represents the polar angle. The green circle represents the numerical aperture of the objective lens.

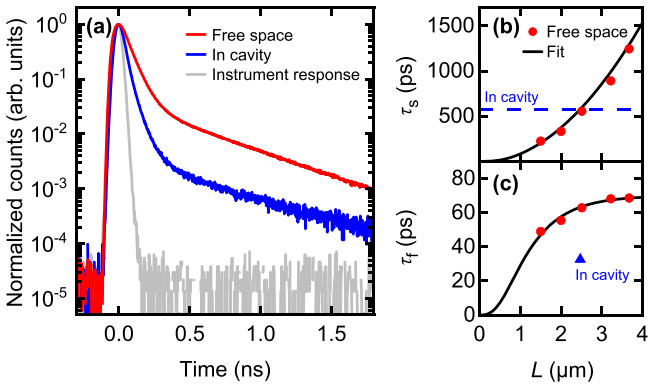

FIG. 4. (a) Decay curves for the Purcell-enhanced nanotube emission from the same device as in Fig. 2 (blue) and a 2.0-μm-long (9,8) nanotube in free space (red). The gray curve is the instrument response function. The excitation powers are 100 nW and 5 nW for nanotubes in the cavity and in free space, respectively. (b), (c) Length dependence of (b) τ_s and (c) τ_f in free space. The red dots are data and the lines are fits using the exciton diffusion model [32]. The blue dashed line in (b) shows the dark exciton lifetime in the cavity, from which we extract the effective nanotube length. The blue triangle in (c) shows the Purcell-accelerated bright exciton lifetime. The laser wavelength and polarization are adjusted to maximize the PL intensity. Wavelength-dependent instrument response is obtained by measuring broadband supercontinuum pulses through a spectrometer with a spectral window of ∼1 nm.

is calculated geometrically by the tube angle with respect to the nanobeam axis [Fig. 2(f), inset], and the width of the cavity mode is taken to be 540 nm. Combining both contributions, we obtain $C_{\mathrm{CNT}} = 1.6$. This analysis results in Purcell factor $F = 0.84 \pm 0.23$ for this device, a reasonable value considering the lateral displacement of ∼0.6 μm [Figs. 2(c) to 2(e)] from the cavity field maxima and the simulation in Figs. 1(c) to 1(e).

In order to estimate the quantum efficiency, we now need to evaluate the acceleration factor by performing time-resolved PL measurements. The same PL microscopy setup is used but the devices are excited with ∼100-fs laser pulses with a repetition rate of 76 MHz and an average power of 100 nW. After spectral rejection of the excitation laser, we couple the emission to a single-mode optical fiber which limits detection to a 1.8-μm diameter spot at the sample. A fiber-coupled superconducting single-photon detector with a timing jitter of 32 ps is used to detect the photons and the decay curves are constructed by time-correlated single-photon counting. Time-resolved PL data taken from the device shown in Fig. 2 is plotted as a blue curve in Fig. 4(a). We observe fast and slow decay components with lifetimes τ_f and τ_s, respectively [32]. By comparing the decay curve to that of a nanotube in free space having a similar length [red curve in Fig. 4(a)], we already see that τ_f corresponding to the bright exciton lifetime is considerably shorter, while τ_s reflecting the dark exciton dynamics is comparable. This is expected as the bright exciton decay is accelerated by the Purcell effect, whereas the dark excitons do not interact with photons and therefore their lifetime would not be changed by the cavity. We note that the contrasting behavior of bright and dark exciton lifetimes rules out extrinsic quenching effects as the cause for bright exciton lifetime shortening. Such effects including quenching caused by contact with the substrate should shorten both bright and dark exciton lifetimes, as in the case for end quenching [32].

We fit the decay curve of the cavity-coupled emission [Fig. 4(a), blue curve] to obtain τ_f and τ_s. A biexponential function convoluted with the instrument response function is used to extract $\tau_f = 34.8 \pm 0.3$ ps, and a single exponential fit to the data in the time range beyond $10\tau_f$ yields $\tau_s = 586 \pm 5$ ps. The change in τ_f for the nanotube coupled to the cavity compared with a nanotube in free space is needed to obtain the value of A, but care must be taken since τ_f is dependent on the nanotube length L [32]. We take advantage of the fact that the dark exciton dynamics is unaffected by the cavity and use the length dependence of τ_s obtained from the exciton diffusion model [32] to determine the nanotube length at which τ_f is compared.

Figures 4(b) and 4(c) show the length dependence of τ_s and τ_f, respectively, for air-suspended (9,8) nanotubes in free space [32]. Both the bright and dark exciton lifetimes increase with the nanotube length due to reduced end quenching in longer nanotubes. By looking up the nanotube length for $\tau_s = 586$ ps [Fig. 4(b), dashed line], $L = 2.5 \pm 0.1$ μm is obtained. The acceleration factor is then evaluated using the corresponding bright exciton lifetime in free space [Fig. 4(c)] and we find $A = 1.82 \pm 0.09$. The error for the acceleration factor is computed from the 1σ confidence intervals of the fits and the standard deviation of the lifetime data in free space. Having determined both F and A for this device, the radiative quantm efficiency of bright excitons is calculated to be 0.98 ± 0.29 using Eq. (1). We may have

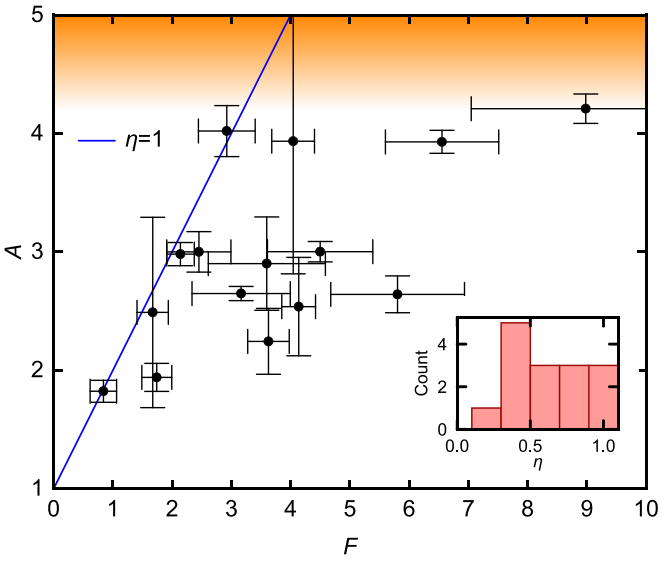

FIG. 5. The acceleration factor as a function of the Purcell factor. The dots are data and the error bars show the 1σ confidence interval. The blue line indicates $\eta = 1$ as given by Eq. (1). Chiralities of the nanotubes in the measured devices are (9,7), (9,8), (10,8), and (11,6), whose τ_f are between 54.6 ps to 64.2 ps in free space. Since the shortest τ_f resolvable by the fitting process is approximately 13 ps, the upper bound of the measurable acceleration factor ranges from 4.2 to 4.9. Inset is the histogram of the radiative quantum efficiences.

overestimated the confidence intervals as $\eta > 1$ would be unphysical, which points to the limits of the assumptions in our model.

The high quantum efficiency is reproducibly observed in a number of devices. We repeated the same measurements in additional devices with varying Purcell factors, and the results are summarized in Supplemental Material S5 [26]. The acceleration factor is plotted as a function of the Purcell factor in Fig. 5, where variations and errors in the measured quantum efficiencies can be seen. The orange shaded area corresponds to the region beyond the shortest resolvable lifetimes. Data points closer to the top-left corner indicate higher quantum efficiency and we observe that the blue line representing unity quantum efficiency passes through a number of data points within the error bars. The inset of Fig. 5 is the histogram of the obtained radiative quantum efficiencies, and 6 out of 15 nanotubes exhibit $\eta > 0.7$. It is not surprising that there are devices showing lower efficiencies since shorter nanotubes have higher nonradiative decay rates (see Supplemental Material Fig. S4 [26]). We may therefore interpret the highest efficiencies observed as being the intrinsic property of the bright excitons in CNTs. Even when considering the error bars of the data points, it is fair to state that their quantum efficiencies are near unity in free space.

The radiative quantum efficiency is directly related to the PL yield, which is defined as a fraction of emitted photons to absorbed photons. The PL yield is not necessarily equal to the radiative quantum efficiency of the bright excitons, as most of the absorbed photons end up in dark excitonic states. There exist 16 exciton states since both the valence and the conduction bands are four-fold degenerate, out of which only one state is bright and all the other states are dark due to spin, momentum, and parity selection rules [33–35]. The initial population of all 16 states should be equal if free carriers are generated as in the case of E_{22} excitation [36] and a PL yield of 6.25% would result for unity quantum efficiency of bright excitons if there are no further population redistribution. Experimentally, a similar value of ∼7% was reported for air-suspended nanotubes at E_{22} excitation [24]. Conversion of the dark excitons to the bright excitons [32] can further increase the PL yields.

We note that air-suspended nanotubes exhibit higher PL yields compared to solution-based nanotubes. There are mainly two reasons for the difference [37]. First, the surfactant molecules can create charge traps that create quenching sites. Second, solution-based tubes are often shorter than those directly synthesized on substrates because of the sonication process and the excitons are more susceptible to quenching at the tube ends. The additional nonradiative decay processes result in lower yields.

It should be possible to enhance the PL yield by choosing excitation methods with higher initial population of bright excitons. Resonant excitation can be used to selectively populate the bright states, and in principle unity PL yield would be achieved. If the rejection of the excitation laser becomes an experimental issue, an alternative is to utilize phonon sidebands [38] and E_{11} excited states [39]. By limiting excitation into the spin singlet manifold, the PL yield is expected to improve by a factor of 4. A more sophisticated scheme will be needed for electrical excitation, such as spin-polarized [40] or energy-selective [41] injection.

Lastly, we would like to comment on the radiative lifetime of excitons in CNTs [34,35,42]. When the radiative quantum efficiency is unity, bright exciton decay time is equivalent to the radiative lifetime. We can therefore consider the reported bright exciton decay times of air-suspended nanotubes ranging from 60 ps to 90 ps [32] to be their effective radiative lifetime at room temperature. In comparison, theoretical calculations [34,35] yielded effective radiative lifetimes to be on the order of 10 ns at room temperature for micelle-wrapped nanotubes, although the dielectric environment is considerably different from those in the air-suspended structures. The experimentally observed bright exciton decay times also show a clear family pattern [32], which has not been addressed theoretically. Updated calculations are needed for an accurate description of radiative lifetimes in air-suspended nanotubes.

In conclusion, we quantitatively estimated the radiative quantum efficiency of bright excitons in air-suspended CNTs. The fraction of the radiative recombination is extracted by utilizing quantum electrodynamical effects in air-mode nanobeam cavities. Combining the Purcell factor characterized from the PL spectra and the acceleration factor obtained from the time-resolved measurements, we find that the radiative quantum efficiency of bright excitons is near unity at room temperature. Our results reveal the intrinsic property of bright excitons in CNTs and demonstrate their true potential for nanoscale photonics. With high-efficiency light emission and single-photon generation capabilities, CNTs may bring breakthroughs in subwavelength silicon photonics and integrated quantum optics.

This work is supported by MIC (SCOPE 191503001), JSPS (KAKENHI JP20H02558, JP20J00817, JP20K15199, JP19J10319), MEXT (Nanotechnology Platform JP-MXP09F19UT0072), and RIKEN (Incentive Research Project). H.M. and D.Y. are supported by JSPS (Research Fellowship for Young Scientists). H.M. acknowledges support from RIKEN (Junior Research Associate Program). We thank H. Kumazaki and T. Tanabe for the transmission measurements. FDTD calculations are performed using the HOKUSAI BigWaterfall supercomputer at RIKEN. We acknowledge the Advanced Manufacturing Support Team at RIKEN for technical assistance.

[1] E. F. Schubert and J. K. Kim, Solid-state light sources getting smart, Science **308**, 1274 (2005).

[2] P. W. Milonni and J. H. Eberly, *Laser Physics* (John Wiley & Sons, New York, 2010), pp. 735–792.

[3] W. M. Steen and J. Mazumder, *Laser Material Processing* (Springer, London, 2010).

[4] H.-W. Chen, J.-H. Lee, B.-Y. Lin, S. Chen, and S.-T. Wu, Liquid crystal display and organic light-emitting diode display: Present status and future perspectives, Light Sci. Appl. **7**, 17168 (2018).

[5] C. Adachi, M. A. Baldo, M. E. Thompson, and S. R. Forrest, Nearly 100% internal phosphorescence efficiency in an organic light-emitting device, J. Appl. Phys. **90**, 5048 (2001).

[6] S. Lamansky, P. Djurovich, D. Murphy, F. Abdel-Razzaq, H.-E. Lee, C. Adachi, P. E. Burrows, S. R. Forrest, and M. E. Thompson, Highly phosphorescent bis-cyclometalated iridium complexes: Synthesis, photophysical characterization, and use in organic light emitting diodes, J. Am. Chem. Soc. **123**, 4304 (2001).

[7] N. M. Gabor, Z. Zhong, K. Bosnick, J. Park, and P. L. McEuen, Extremely efficient multiple electron-hole pair generation in carbon nanotube photodiodes, Science **325**, 1367 (2009).

[8] D. R. McCulley, M. J. Senger, A. Bertoni, V. Perebeinos, and E. D. Minot, Extremely efficient photocurrent generation in carbon nanotube photodiodes enabled by a strong axial electric field, Nano Lett. **20**, 433 (2020).

[9] N. Higashide, M. Yoshida, T. Uda, A. Ishii, and Y. K. Kato, Cold exciton electroluminescence from air-suspended carbon nanotube split-gate devices, Appl. Phys. Lett. **110**, 191101 (2017).

[10] A. Graf, M. Held, Y. Zakharko, L. Tropf, M. C. Gather, and J. Zaumseil, Electrical pumping and tuning of exciton-polaritons in carbon nanotube microcavities, Nat. Mater. **16**, 911 (2017).

[11] X. Ma, N. F. Hartmann, J. K. S. Baldwin, S. K. Doorn, and H. Htoon, Room-temperature single-photon generation from solitary dopants of carbon nanotubes, Nat. Nanotechnol. **10**, 671 (2015).

[12] A. Ishii, T. Uda, and Y. K. Kato, Room-temperature single-photon emission from micrometer-long air-suspended carbon nanotubes, Phys. Rev. Appl. **8**, 054039 (2017).

[13] X. He, H. Htoon, S. K. Doorn, W. H. P. Pernice, F. Pyatkov, R. Krupke, A. Jeantet, Y. Chassagneux, and C. Voisin, Carbon nanotubes as emerging quantum-light sources, Nat. Mater. **17**, 663 (2018).

[14] R. Miura, S. Imamura, R. Ohta, A. Ishii, X. Liu, T. Shimada, S. Iwamoto, Y. Arakawa, and Y. K. Kato, Ultralow mode-volume photonic crystal nanobeam cavities for high-efficiency coupling to individual carbon nanotube emitters, Nat. Commun. **5**, 5580 (2014).

[15] F. Pyatkov, V. Fütterling, S. Khasminskaya, B. S. Flavel, F. Hennrich, M. M. Kappes, R. Krupke, and W. H. P. Pernice, Cavity-enhanced light emission from electrically driven carbon nanotubes, Nat. Photonics **10**, 420 (2016).

[16] A. Ishii, X. He, N. F. Hartmann, H. Machiya, H. Htoon, S. K. Doorn, and Y. K. Kato, Enhanced single photon emission from carbon nanotube dopant states coupled to silicon microcavities, Nano Lett. **18**, 3873 (2018).

[17] H. Machiya, T. Uda, A. Ishii, and Y. K. Kato, Spectral tuning of optical coupling between air-mode nanobeam cavities and individual carbon nanotubes, Appl. Phys. Lett. **112**, 021101 (2018).

[18] A. Noury, X. L. Roux, L. Vivien, and N. Izard, Enhanced light emission from carbon nanotubes integrated in silicon microresonator, Nanotechnology **26**, 345201 (2015).

[19] N. Higuchi, H. Niiyama, K. Nakagawa, and H. Maki, Efficient and narrow-linewidth photoluminescence devices based on single-walled carbon nanotubes and silicon photonics, ACS Appl. Nano Mater. **3**, 7678 (2020).

[20] S. Khasminskaya, F. Pyatkov, K. Słowik, S. Ferrari, O. Kahl, V. Kovalyuk, P. Rath, A. Vetter, F. Hennrich, M. M. Kappes, G. Gol'tsman, A. Korneev, C. Rockstuhl, R. Krupke, and W. H. Pernice, Fully integrated quantum photonic circuit with an electrically driven light source, Nat. Photonics **10**, 727 (2016).

[21] E. M. Purcell, Spontaneous emission probabilities at radio frequencies, Phys. Rev. **69**, 681 (1946).

[22] A. Jeantet, Y. Chassagneux, C. Raynaud, P. Roussignol, J. S. Lauret, B. Besga, J. Estève, J. Reichel, and C. Voisin, Widely Tunable Single-Photon Source from a Carbon Nanotube in the Purcell Regime, Phys. Rev. Lett. **116**, 247402 (2016).

[23] Y. Luo, E. D. Ahmadi, K. Shayan, Y. Ma, K. S. Mistry, C. Zhang, J. Hone, J. L. Blackburn, and S. Strauf, Purcell-enhanced quantum yield from carbon nanotube excitons coupled to plasmonic nanocavities, Nat. Commun. **8**, 1413 (2017).

[24] J. Lefebvre, D. G. Austing, J. Bond, and P. Finnie, Photoluminescence Imaging of Suspended Single-Walled Carbon Nanotubes, Nano Lett. **6**, 1603 (2006).

[25] A. F. Oskooi, D. Roundy, M. Ibanescu, P. Bermel, J. Joannopoulos, and S. G. Johnson, Meep: A flexible free-software package for electromagnetic simulations by the FDTD method, Comput. Phys. Commun. **181**, 687 (2010).

[26] See Supplemental Material at http://link.aps.org/supplemental/10.1103/PhysRevResearch.4.L022011 for a schematic showing the parameters of nanobeam cavities, PL line scans along the nanobeam cavities, the characterization of the cavity quality factor, a discussion of the collection efficiencies, a summary table of the Purcell and acceleration factors, and the length dependence of the radiative quantum efficiency.

[27] I. Sarpkaya, Z. Zhang, W. Walden-Newman, X. Wang, J. Hone, C. W. Wong, and S. Strauf, Prolonged spontaneous

emission and dephasing of localized excitons in air-bridged carbon nanotubes, Nat. Commun. **4**, 2152 (2013).

[28] A. Ishii, M. Yoshida, and Y. K. Kato, Exciton diffusion, end quenching, and exciton-exciton annihilation in individual air-suspended carbon nanotubes, Phys. Rev. B **91**, 125427 (2015).

[29] P. H. Tan, A. G. Rozhin, T. Hasan, P. Hu, V. Scardaci, W. I. Milne, and A. C. Ferrari, Photoluminescence Spectroscopy of Carbon Nanotube Bundles: Evidence for Exciton Energy Transfer, Phys. Rev. Lett. **99**, 137402 (2007).

[30] K. Matsuda, Y. Kanemitsu, K. Irie, T. Saiki, T. Someya, S. Miyauchi, and S. Maruyama, Photoluminescence intermittency in an individual single-walled carbon nanotube at room temperature, Appl. Phys. Lett. **86**, 123116 (2005).

[31] Q. Quan and M. Loncar, Deterministic design of wavelength scale, ultra-high Q photonic crystal nanobeam cavities, Opt. Express **19**, 18529 (2011).

[32] A. Ishii, H. Machiya, and Y. K. Kato, High Efficiency Dark-To-Bright Exciton Conversion in Carbon Nanotubes, Phys. Rev. X **9**, 041048 (2019).

[33] Y. Miyauchi, Photoluminescence studies on exciton photophysics in carbon nanotubes, J. Mater. Chem. C **1**, 6499 (2013).

[34] V. Perebeinos, J. Tersoff, and P. Avouris, Radiative Lifetime of Excitons in Carbon Nanotubes, Nano Lett. **5**, 2495 (2005).

[35] C. D. Spataru, S. Ismail-Beigi, R. B. Capaz, and S. G. Louie, Theory and *ab initio* Calculation of Radiative Lifetime of Excitons in Semiconducting Carbon Nanotubes, Phys. Rev. Lett. **95**, 247402 (2005).

[36] Y. Kumamoto, M. Yoshida, A. Ishii, A. Yokoyama, T. Shimada, and Y. K. Kato, Spontaneous Exciton Dissociation in Carbon Nanotubes, Phys. Rev. Lett. **112**, 117401 (2014).

[37] T. Hertel, S. Himmelein, T. Ackermann, D. Stich, and J. Crochet, Diffusion Limited Photoluminescence Quantum Yields in 1-D Semiconductors: Single-Wall Carbon Nanotubes, ACS Nano **4**, 7161 (2010).

[38] O. N. Torrens, M. Zheng, and J. M. Kikkawa, Energy of K-Momentum Dark Excitons in Carbon Nanotubes by Optical Spectroscopy, Phys. Rev. Lett. **101**, 157401 (2008).

[39] J. Lefebvre and P. Finnie, Excited Excitonic States in Single-Walled Carbon Nanotubes, Nano Lett. **8**, 1890 (2008).

[40] J. Wang, A. Chepelianskii, F. Gao, and N. C. Greenham, Control of exciton spin statistics through spin polarization in organic optoelectronic devices, Nat. Commun. **3**, 1191 (2012).

[41] K. Kimura, K. Miwa, H. Imada, M. Imai-Imada, S. Kawahara, J. Takeya, M. Kawai, M. Galperin, and Y. Kim, Selective triplet exciton formation in a single molecule, Nature (London) **570**, 210 (2019).

[42] Y. Miyauchi, H. Hirori, K. Matsuda, and Y. Kanemitsu, Radiative lifetimes and coherence lengths of one-dimensional excitons in single-walled carbon nanotubes, Phys. Rev. B **80**, 081410(R) (2009).